Thermal Effects in Dynamic Storage of Hydrogen by Adsorption

Malek Lamari, Asdin Aoufi, and Pierre Malbrunot
LIMHP−CNRS, Av. J.B. Clément, Villetaneuse, France 93430

Thermal effects in dynamic hydrogen storage by adsorption at room temperature and high pressure are studied theoretically and experimentally. The system of adsorbate−adsorbent used was hydrogen in granular activated carbon. The theoretical analysis was based on heat- and mass-transfer modeling in a packed-bed adsorber, with particular emphasis on the thermal effects occurring during charge and discharge steps. The influence of gas flow rate and storage pressure (up to 15 MPa) on the total amount stored or delivered was investigated. Operating conditions were compatible with practical application for onboard vehicle storage. The experimental study was carried out in cylindrical 2-L reservoirs filled with granular activated carbon in which the bed temperature was measured at various positions. The temperature changes during both charge and discharge agreed well with the model predictions.

Introduction

Hydrogen utilization is receiving increased attention in view of the importance of the world's demand for energy caused by the simultaneous growth of the world population and of air-pollutant emissions produced by carbonaceous fuels. As alternative energy, it is the cleanest fuel, and is especially attractive for electric-vehicle use (Nicholetti, 1995). Important properties of hydrogen such as heat power (2.75 times higher than gasoline for the same weight) make it an ideal candidate for transport applications (Das, 1996). A more difficult issue facing the transition to its effective utilization is onboard storage; this may influence the vehicle's cost, performance, and fuel economy (Berry and Aceves, 1998; Noh et al., 1987; Hynek et al., 1997).

There are currently four main technologies for onboard vehicle hydrogen storage: compressed gas, liquefaction, metal hydrides, and adsorption. Particular attention was focused on carbon sorption systems, since they can store hydrogen of moderate size, weight, and pressure (Chahine and Bénard, 1998; Lamari et al., 1997; Chahine and Bose, 1992). Indeed, when the gas is introduced into a container, a large part of it is stored by adsorption and the rest by compression. This contributes to reducing the operating pressure compared to compressed gas technology. Consequently, less weight is required and better security is ensured. This application has been enhanced by the discovery of new graphitic structure materials: nanotubes and nanofibers are considered promising storage adsorbents (Chambers et al., 1998; Dillon et al., 1997; Rodriguez et al., 1997). However, practical difficulties, such as temperature changes in dynamic charge or discharge that requires thermal control, exist in the storage process.

Considering packed-bed pressurization (charge) and depressurization (discharge), there are two main heat effects: heat released by adsorption and by compression, and reverse temperature drop due to decompression and desorption. This may have a detrimental effect on performance of the storage system during both cycles (Barbosa et al., 1997a; Chang and Talu, 1996). A lower amount of gas is stored at the target pressure during the first operation and a residual amount of stored gas is retained in the container at the depletion pressure during the second operation.

Several theoretical and experimental studies (Kikkinides and Yang, 1993; Lu et al., 1993; Zhong et al., 1992; Sundaram and Wanket, 1988; Farooq et al., 1988) describing the thermal effects associated with adsorption have been carried out, particularly in the field of pressure swing adsorption processes (PSA), which are currently used in gas separation and

---

Correspondence concerning this article should be addressed to M. Lamari.

purification. Those studies differ from storage processes in essential features: one component only, noncontinuous flow, high pressure, only one bed entrance to adsorb and desorb the gas. Furthermore, charge and discharge steps involve rapid pressure change, as well as a high large pressure drop at the bed entrance. These specific features induce additional difficulties in modeling, especially stiff pressure variations.

The main objective of this work is the investigation of thermal effects during high-pressure charge and discharge in the adsorbent packed bed for the storage reservoir. This is essential to control fueling processes and for manufacturing on-board storage vehicle reservoirs. In the first part of this article, we elaborate a theoretical study of the dynamic storage of hydrogen by adsorption on activated carbon at room temperature and high pressures. We have developed two models in order to successively evaluate overheating and cooling inside the column during charge and discharge. The charge model includes mass and energy balances with incorporation of a valve equation, making it appropriate for modeling storage systems with wide charge pressure variation. For the discharge model, an adaptation of the model proposed by Chang and Talu (1996) is developed. In the second part of this work, the experimental study of this system is presented. The influence of the flow rate and storage pressure on temperature variations is investigated in a range of pressures from 5 to 15 MPa. In the third part, experimental and modeling results are compared and discussed.

Mathematical Modeling

Description of the storage system

In order to reproduce conditions similar to those of hydrogen in practical application—(1) at the fuel station, by supplying the vehicle reservoir during the charge stage, and (2) for the fuel cell or engine motor, the imposed flow gas demand during discharge stage—the same scenario is represented. Figure 1 shows the storage system considered here. It consists of a cylindrical reservoir filled with a packed bed of porous adsorbent particles. The gas enters and leaves through a small opening at the center of the reservoir top. During the charge step, a hydrogen flow continuously supplies the bed at constant high pressure until the target pressure is obtained in the cylinder. At a given feeding pressure, the time of charge is dictated by the flow rate, which is controlled by the manual opening micrometering valve. The flow rate is dependent on the pressure drop in the entrance region and decreases down to zero at the preset pressure. On the other hand, during the discharge step, the gas is desorbed and expanded to atmospheric pressure at a constant gas flow rate. For this reason, we have developed two distinct models: one for charge, where the flow rate varies with the pressure, and one for discharge, where the gas flow rate is constant.

The charge step in the practical reservoir filling conditions is fast enough to make (in a first approximation) the heat exchange with the surroundings negligible, and the important temperature gradients are in the axial direction. On the other hand, as demonstrated by Barbosa et al. (1997b), intragranular mass-transfer resistance also has to be taken into account. The diffusional resistance influences the final filling time (that is, the time that the storage pressure is reached). This aspect is discussed in detail in the modeling results section.

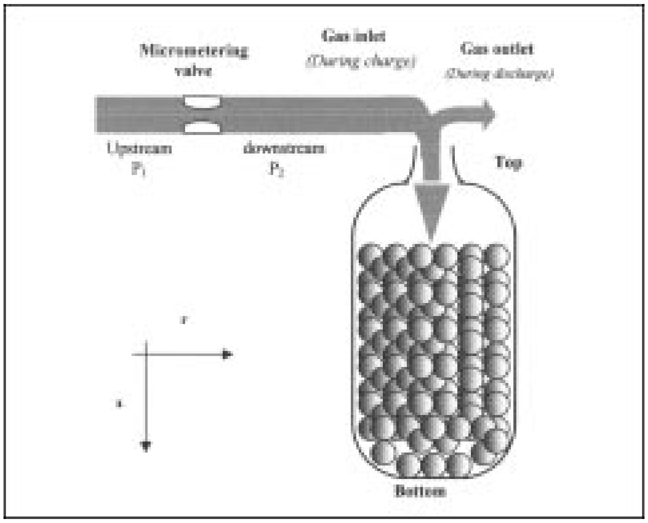

Figure 1. Process description for charge and discharge models.

The discharge step is slow enough in vehicle running conditions to allow instantaneous equilibrium assumption. Furthermore, the temperature variation is predominantly influenced by heat transfer in the radial direction, due to heat exchange with the surroundings. If the cylinder is long enough, the axial temperature variation can also be neglected (Barbosa, 1995).

Charge model

Assumptions. For modeling the charge step described earlier, the following assumptions were made:

1. Initially the bed is at a uniform temperature and at an atmospheric pressure of H_2.

2. The gas behavior is assumed to be ideal. This approximation is reasonable in view of the slight variation in its compressibility factor in the pressure and temperature range of interest. From 0.1 MPa to 15 MPa, the variation is less than 8%.

3. The cylindrical adsorbent particles in the experimental column are presumed to be spherical with an equivalent diameter (based on surface, $d_p = 6.42 \times 10^{-3}$ m).

4. One-dimensional formulation is made in the axial direction for density and temperature.

5. Linear variation of gas velocity exists along the bed.

6. The mass-transfer resistance in the particle is approximated by using the linear driving force (LDF) (Glueckauf, 1955) in order to represent the mass-transfer rate. Its validity in this work is justified because of $(D_e t_c / r_p^2) > 0.1$ (Yang, 1987) and the modest curvature of the isotherms (Hassan et al., 1985). The gas-film diffusion resistance is neglected.

According to the preceding assumptions, the mass and heat equations are written as follows:

Mass Balance.

$$\underset{\substack{\text{accumulation}\\ \text{rate of gas}}}{\frac{\partial\rho}{\partial t}} + \underset{\substack{\text{convective flux and}\\ \text{axial dispersion}}}{\frac{\partial}{\partial x}\left[u\rho - D_{ax}\frac{\partial\rho}{\partial x}\right]} + \underset{\text{rate of gas adsorption}}{\left(\frac{1-\epsilon}{\epsilon}\right)\rho_s M_{\mathrm{H}_2}\frac{\partial q(x,t)}{\partial t}} = 0. \quad (1)$$

Energy Balance.

$$\frac{\partial}{\partial t}\left[\underset{\substack{\text{rate of heat}\\ \text{accumulation}\\ \text{in the bulk gas}}}{\frac{A_1}{A}\rho C_p T} + \underset{\substack{\text{rate of heat}\\ \text{accumulation}\\ \text{in the adsorbent}}}{\frac{A_1}{A}\left(\frac{1-\epsilon}{\epsilon}\right)\rho_s C_{ps} T} + \underset{\substack{\text{rate of heat}\\ \text{accumulation}\\ \text{in the wall}}}{\frac{A_2}{\epsilon A}\rho_w C_{pw} T} \underset{\substack{\text{heat}\\ \text{generated by}\\ \text{compression}}}{- r_g \rho T}\right] - \underset{\substack{\text{heat generated}\\ \text{by adsorption}}}{\left(\frac{1-\epsilon}{\epsilon}\right)\Delta H \rho_s \frac{\partial q(x,t)}{\partial t}}$$

$$= \frac{\partial}{\partial x}\left[\underset{\substack{\text{conduction}\\ \text{heat flux}\\ \text{in the bed}}}{\frac{A_1}{\epsilon A}\lambda_b\frac{\partial T}{\partial x}} + \underset{\substack{\text{conduction heat}\\ \text{flux in the wall}}}{\frac{A_2}{\epsilon A}\lambda_w\frac{\partial T}{\partial x}} - \underset{\substack{\text{convection}\\ \text{heat flux}}}{\rho C_p u T}\right] - \underset{\substack{\text{external heat}\\ \text{transfer}}}{\frac{4h}{\epsilon D_0}(T - T_0)}. \quad (2)$$

Initial and Boundary Conditions. The initial conditions for the charge startup desorbed bed are

$$\rho(x,t=0) = \rho_0; \qquad T(x,t=0) = T_0;$$

$$q(x,t=0) = q(T_0 = 293\ K,\ P_0 = 0.1\ \text{MPa}). \quad (3)$$

The boundary conditions are

$$x = 0: \quad u\rho(0,t) - D_{ax}\frac{\partial\rho}{\partial x}(0,t) = u\rho_0; \quad T(0,t) = T_0 \quad (4)$$

$$x = L: \quad \frac{\partial\rho}{\partial x}(L,t) = 0; \quad \frac{\partial T}{\partial x}(L,t) = 0. \quad (5)$$

Intraparticle Mass Transfer. Overall mass transfer between the solid and gas phase is expressed by the LDF adsorption rate:

$$\frac{\partial q(x,t)}{\partial t} = ka_s[q^*(\rho,T) - q(x,t)], \quad (6)$$

where q is the amount of gas adsorbed in the particle, q^* is the amount adsorbed in equilibrium with the gas-phase density outside the particle, and ka_s ($ka_s = 15D_e/r_p^2$) is the product of external-particle mass-transfer coefficient and the specific area.

Valve Equation. The inlet velocity ($x = 0$) is determined from the valve equation (VE). The works of Chou and Huang (1994a,b) and Kumar (1989) used this approach at low pressure ($\sim$0.3 MPa) in PSA air separation. They demonstrated that VE showed good agreement with the PSA experimental data, leading to the prediction of the inlet and outlet flow rate of the bed through the valve connection. Here, we extend and validate its applicability experimentally at high pressure between 5 and 15 MPa. The following formula is recommended for gases by the Fluids Controls Institute Inc., given by the manufacturer's (Autoclave Engineers, Pennsylvania, USA) technical information:

$$Q = 77.01 \times 10^{-8} c_v \left[\frac{(P_1^2 - P_2^2)}{S_G T}\right]^{1/2} \quad \text{for} \quad P_2 > 0.53P_1 \quad (7)$$

or

$$Q = 65.31 \times 10^{-8} c_v P_1 \left(\frac{1}{S_G T}\right)^{1/2} \quad \text{for} \quad P_2 \le 0.53P_1, \quad (8)$$

where

Q = flow rate through the micrometering valve (VL on Figure 4) in $\mathrm{m^3/s}$
c_v = valve flow coefficient
S_G = specific gravity of gas (hydrogen density/air density)
T = absolute temperature of flowing gas (K)
P_1 = upstream pressure (Pa) (fixed)
P_2 = downstream pressure (Pa) (bed pressure)

Discharge model

Based on work by Chang and Talu (1996), a radial one-dimensional model of column discharge is used (see preceding discussion). But this model has to be adapted to our conditions. In their model, the mass accumulation of methane in the gas phase was neglected because its contribution never exceeded 15% of the total contents of the column. In the case of hydrogen storage at room temperature and moderate pressure, the bulk accumulation (compressed gas) is between 40 and 70% (depending on the adsorbent) of the total amount stored, and consequently it must be taken into account in mass and energy equations (Malbrunot et al., 1996).

Assumptions. In this work, a more detailed model is suggested with the following assumptions:

1. Initially, the discharge starts at charge end conditions: high pressure (5, 10, or 15 MPa) with uniform temperature and gas density in the bed.
2. Instantaneous equilibrium: the mass-transfer resistance between adsorbed and gaseous hydrogen can be neglected because the discharge process is slow enough and is governed by the energy demand of the vehicle. Consequently, the discharge duration is increased, compared to the charge step.
3. Temperature and density are uniform in the axial direction and variations exist in the radial direction. Because the flow rate is lower, the heat transfer becomes more significant between the column and the ambience.

Assumptions 2 and 3 in the charge model are also assumed in the discharge model.

Mass Balance.

$$\frac{f}{L} = (1-\epsilon)\rho_s \frac{\partial q}{\partial t} + \frac{\epsilon}{M_{H_2}} \frac{\partial \rho}{\partial t}, \tag{9}$$

where f is the specific molar flux in the column and is related to the mass flow-rate demand of the system $\dot{m}$:

$$\dot{m} = \pi R^2 M_{H_2} f. \tag{10}$$

Energy Balance.

$$\frac{\partial}{\partial t}\left[\underbrace{\rho C_p T}_{\substack{\text{rate of heat}\\ \text{accumulation}\\ \text{in the bulk}\\ \text{gas}}} + \underbrace{\frac{(1-\epsilon)}{\epsilon}\rho_s C_{ps} T}_{\substack{\text{rate of heat}\\ \text{accumulation}\\ \text{in the adsorbent}}} - \underbrace{r_g \rho T}_{\substack{\text{heat}\\ \text{necessary}\\ \text{for}\\ \text{decompression}}} \right]$$

$$- \underbrace{\frac{(1-\epsilon)}{\epsilon}\rho_s \Delta H \frac{\partial q}{\partial t}}_{\substack{\text{energy necessary}\\ \text{for desorption}}} = \underbrace{\frac{\lambda_b}{\epsilon r}\frac{\partial}{\partial r}\left(r\frac{\partial T}{\partial r}\right)}_{\substack{\text{bed conduction}\\ \text{heat transfer}}}$$

$$+ \underbrace{\frac{\lambda_w}{\epsilon r}\frac{\partial}{\partial r}\left(r\frac{\partial T}{\partial r}\right)}_{\substack{\text{wall conduction}\\ \text{heat transfer}}} - \underbrace{\frac{f}{\epsilon L} C_p M_{H_2}(T - T_0)}_{\substack{\text{heat removed from}\\ \text{the column}}}. \tag{11}$$

Initial and Boundary Conditions. The initial conditions are

$$t = 0 \quad q = f(T, P) \quad \text{charge condition} \tag{12}$$

$$\rho = \rho_0;\ T = T_0 = 293.15\ \text{K},\ P = P_0 \tag{13}$$

The boundary conditions are

$$r = 0 \quad \frac{\partial T}{\partial r}(0, t) = 0 \quad (\text{symmetry condition}). \tag{14}$$

The second boundary condition is determined by the energy balance on the cylinder wall:

$$r = R \quad - \underbrace{\lambda_b \frac{\partial T}{\partial r}(R, t)}_{\substack{\text{bed heat}\\ \text{diffusion flux}}} - \underbrace{\lambda_w \frac{\partial T}{\partial r}(R, t)}_{\substack{\text{wall heat}\\ \text{diffusion flux}}}$$

$$= \underbrace{w C_{pw} \rho_w \frac{\partial T}{\partial t}(R, t)}_{\substack{\text{wall heat}\\ \text{accumulation}}} + \underbrace{h[T(R, t) - T_0]}_{\substack{\text{external heat}\\ \text{transfer}}}. \tag{15}$$

Estimation of Equilibrium and Transfer Parameters

One of the main difficulties in running these predictive models is to accurately determine the equilibrium, heat-, and mass-transfer parameters inside the column. The data available in the literature are not suitable to our specific system (high pressure, hydrogen, given adsorbent); therefore, when possible, the parameters were measured in this study.

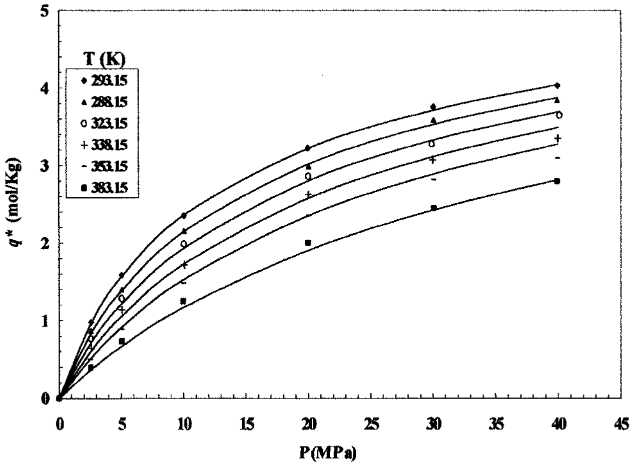

Figure 2. Hydrogen adsorption isotherm.

Adsorption isotherm

Hydrogen adsorption isotherms at high pressure were measured by a mixed gravimetric and volumetric method over the temperature range of 293.15–383.15 K (every 15 K: seven isotherms). The maximum pressure reached for each of these isotherms was about 40 MPa. A cell of volume V_{cell} was held under a high accurate balance, capable of weighing up to 2 kg, with a sensitivity of 10^{-3} kg. To ensure the pressurization, this cell was connected to a high-pressure circuit by a long stainless-steel capillary tube (0.5×10^{-3} m diameter and 1.6 m long): one end was rigidly fixed and the other end was hung with the cell on the balance. With this device, the elastic force of the capillary tube is less than the balance sensitivity.

The cell was filled with the adsorbent previously out-gassed in a secondary vacuum at 573.15 K for 24 h. Hydrogen was introduced up to the target pressure and the weight was noted at the thermodynamic equilibrium reached. Finally, from the knowledge of helium density of the adsorbent, mass-balance equation, and *PVT* relationships, the amount of excess adsorption was calculated. More details about the adsorbent helium density are published elsewhere (Malbrunot et al., 1997; Darkrim et al., 1999).

The experimental results are presented in Figure 2. The collected data were correlated with the Radke-Prausnitz isotherm equation (Radke and Prausnitz, 1972).

$$q^*(P, T) = \frac{F K(T) P}{\left(F + K(T) P^{1-n}\right)}, \tag{16}$$

where

$$K(T) = K_0 \exp\left(-B\frac{\Delta H}{RT}\right). \tag{17}$$

As shown in Figure 2, the experimental data were successfully fitted with the preceding equation. The fitted constant values are listed for the best fits (~ 2%) in Table 1.

Table 1. Constants for Radke–Prausnitz Isotherm and Enskog Equations for Hydrogen

Eqs. 16–17	
F	2.9634
B	-1.0×10^{-5}
K_0	2.0778
n	89.6890×10^{-2}
ΔH	10.5×10^{3} J/mol
Eq. 22	
σ	2.915 Å
ϵ/k	38 K
$\Omega^{(1,1)}$	0.7896

Table 2. Parameter Values Used in the Model Calculations

Column length	487×10^{-3} m
Column diameter	78.5×10^{-3} m
Column wall thickness	5.75×10^{-3} m
Bed voidage (ϵ)	0.4
Granular carbon	Adsorbent AC35
Equivalent particle diameter	6.42×10^{-3} m
Particle density (ρ_s)	9.6×10^{2} kg/m^3
Wall density	7930 kg/m^3
Particle porosity (ϵ_p)	5.7×10^{-1}
Bed density	4.6×10^{2} kg/m^3
Dispersion coefficient (D_{ax})*	3.38×10^{-5} m^2/s
Diffusional time constant of H_2 (D_e/R_p^2)	2.98×10^{-2} s^{-1}
Heat-transfer coefficient (h)	12 W/K·m^2
Bed stagnant thermal conductivity (λ_b^0)	7.64×10^{-1} W/m·K
Wall thermal conductivity	16.03 W/m·K
Solid heat capacity (C_{ps})	7.039×10^{2} J/kg·K
Gas heat capacity (C_p)	14.42×10^{3} J/kg·K
Wall heat capacity (C_{pw})	5.02×10^{2} J/kg·K
Adsorption heat (ΔH)	10.5×10^{3} J/mol

*Gunn (1987).

Valve flow coefficient

During the charge step, the feed gas at constant pressure P_1 was expanded to P_2 through a fixed-opening micrometering valve (Figure 1). Figure 3 shows the experimental results at $P_1 = 10$ MPa and for different flow rates measured with an accurate volumetric flowmeter. The valve coefficient c_v was adjusted for each flow rate. In all cases, the flow rate remained constant when $P_1 < 0.53\ P_2$. Small c_v values were obtained on the order of 10^{-3}. They were ten times smaller than the values of Chou and Huang (1994a). This difference could be explained by the high ratio pressure (>5) between feed pressure and downstream pressure in this work (lower than 0.3 in the Chou and Huang work).

Effective thermal conductivity

The bed effective thermal conductivity λ_b was determined by the following relation (Froment and Bischoff, 1990):

$$\lambda_b = \lambda_b^0 + \lambda_b^c, \tag{18}$$

where the thermal conductivity due to convective transport λ_b^c was given by the correlation

$$\lambda_b^c = 0.12\,PrRe. \tag{19}$$

The stagnant thermal conductivity λ_b^0 was estimated by the minimization of the difference between calculated and measured temperatures. For experiments, the transient method was used (Lamari et al., 1999), in which the stagnant hydrogen and the adsorbent contained in the cell were heated up to the preset temperature. The temperature history was recorded at the center and at the wall of the bed. The experiments were carried out successively at 5, 10, and 15 MPa. The calculation was based on the numerical solution of the unsteady-state energy equation. The stagnant thermal conductivity obtained λ_b^0 was about 0.76 W/m·K (see Table 2). The pressure effect was on the order of 1%, and could therefore be neglected in calculating λ_b.

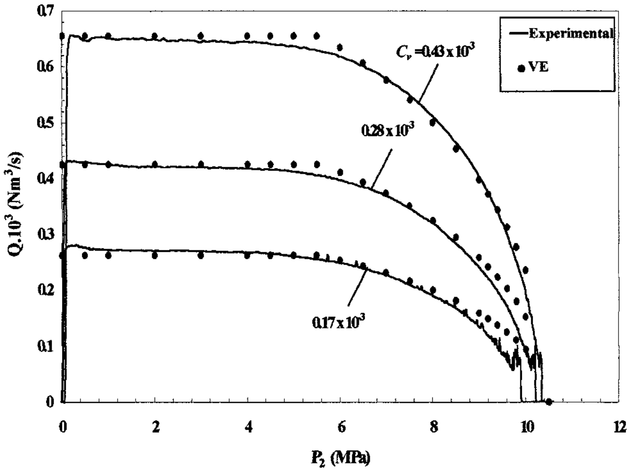

Figure 3. Comparison of calculated and experimental flow rate vs. pressure for different valve coefficients at 10 MPa.

Effective self-diffusivity for single component

The effective self-diffusivity D_e was estimated by a simple empirical method correlation given by Yang and Liu (1982) (see Eq. 6):

$$D_e = \epsilon_p \frac{D}{\tau}, \tag{20}$$

where ϵ_p is the intraparticle void fraction τ is the tortuosity factor; and D is the diffusivity

$$D = \left(\frac{1}{D_m} + \frac{1}{D_k}\right)^{-1}, \tag{21}$$

where D_m is the molecular diffusivity and D_k is the Knudsen diffusivity in m^2/s.

At high operating pressures the contribution of Knudsen diffusion became smaller (Ruthven et al., 1994), and $D \to D_m^*$.

In our case, the value of D_k was estimated and was three orders of magnitude lower than D_m. Hence, here we considered only the molecular diffusion for calculating the effective coefficient D_e, by application of the Enskog relationship (Hirschfelder et al., 1964):

$$D_m = 0.026280 \frac{\sqrt{T^3/M_{\mathrm{H}_2}}}{P\sigma^2 \Omega^{(1,1)\otimes}(T^*)}, \tag{22}$$

where

D_m = molecular diffusion for self-diffusion case (m^2/s)
P = pressure (Pa)
T = temperature (K)
T^* = reduced temperature ($= kT/\epsilon$)
σ, ϵ/k = parameter in Lennard-Jones potential function (Å, K)
$\Omega^{(1,1)}$ = collision integral function

Heat of adsorption

A widely used method is to determine the isosteric heat of adsorption by application of the Clausius-Clapeyron equation (Brunauer, 1945). This equation relates the adsorption heat effects to the temperature dependence of the adsorption isotherm. For this purpose, the data in Figure 2 were plotted in the form of $\ln P$ vs. $1/T$, and thereafter heat of adsorption ΔH was obtained from the local slopes of the curves. The heat of adsorption ΔH varied slightly with the adsorbed amount and the temperature (less than 5%) in the range of our operating conditions. For model calculations, we used an average value of ΔH.

Solution technique

The mutual coupling between the mass- and heat-transfer equations exhibits some stiffness and requires a specific temporal discretization. We chose the implicit backward Euler scheme (Fletcher, 1991), which is unconditionally stable and well suited for the treatment of such stiff phenomena. A constant time step is used throughout the numerical computations.

The mass and heat balances are nonlinear convection-diffusion equations written in conservation form. A critical aspect of the discretization of these equation types is the accurate numerical evaluation of the nonlinear convection term. The use of an upwind scheme induces numerical diffusion monitored by the local Peclet number. This numerical diffusion will significantly alter the temperature profiles in important convective flows. In order to avoid such problems, a straightforward centered scheme was applied with a sufficiently dense mesh. The solution was advanced in time, using an iterative procedure that involved the inversion of two tridiagonal systems, efficiently performed by forward–backward Thomas' algorithm (Fletcher, 1991). During the iterative procedure, the velocity, temperature and density profiles were updated until convergence was achieved with a relative criterion of 10^{-9}. We notice that complete simulation takes up to 300 s on an Indigo2 R8K SGI workstation. The accuracy of the numerical solution is confirmed by dividing the time step and spatial mesh by 2 until the computed profiles remain unchanged.

Experimental Studies

Apparatus and materials

To verify the validity of the proposed models an experimental device was constructed (Figure 4). The system consisted of two main circuits: (1) charge, and (2) discharge. A volumetric flowmeter (FTO) with a reading accuracy of $\pm 0.3\%$, manufactured by EG&G (model 1INIR3-PHC-5), was used to adjust and measure the charge flow rate under operating pressure. The Smart Flow Transmitter connected to the FTO enabled correction of the gas flow rate instantaneously with temperature and pressure variation. Upstream, a micrometering valve was used in order to obtain an adjustable and reproductive flow. The adsorption column was a laboratory-scale (2-L) stainless-steel cylinder (485×10^{-3} m long; 78.5×10^{-3} m diameter). Its geometric shape was similar to that of the commercial gas cylinder.

In most experiments, the external wall was directly in contact with ambient air, that is, in the usual conditions. In other particular cases: (1) a coil was wound around the column in which thermostatted water circulated to ensure fixed external wall temperature at 293 K; (2) the column was insulated by fiberglass to ensure near adiabatic conditions.

The column was packed with commercial activated-carbon particles (AC35, CECA—France) of cylindrical shape (3.5×10^{-3} m diameter; 10^{-2} m long). This adsorbent has an average surface area of 1,000 $m^2 \cdot g^{-1}$ and a bulk density of 460 $kg \cdot m^{-3}$. As shown in Figure 5, six iron/copper/nickel thermocouples were placed along the column to obtain radial and axial temperature profiles. The pressure was measured by the Heise digital pressure transducer (model ATS 2000, precision: $\pm 0.02\%$ of the full scale). A mass flow controller (MFC) (type 1500, precision: $\pm 0.1\%$ of the full scale) manufactured by MKS was used during the discharge stage. This apparatus operates at constant pressure regulated to 0.15 MPa by the pressure regulator M2. All devices—the FTO, MFC, pressure transducer, and thermocouples—were linked to the interface (model Keithley 2000) and recorded in the computer at a 0.25-s time interval. The set data were analyzed by means of the HPVEE (HP Visual Environment Engineering) software program.

Procedures

Experiments were carried out at three different pressures: 5, 10, and 15 MPa. The main experimental parameters were: (1) for charge, the initial gas flow rate that governs the complete fill duration; and (2) for discharge, the constant flow rate that governs the available power. This flow rate can be regulated between 0.11×10^{-3} and 0.91×10^{-3} Nm^3/s for a charge that corresponds to a vehicle fill-up time of between 300 and 1,200 s, and between 0.54×10^{-3} and 0.0938×10^{-3} Nm^3/s for a discharge that corresponds to a different energy demand of the engine. Before each experiment, the cylinder was desorbed using a primary vacuum pump.

Charge. During this step, the gas was introduced into the column via the pneumatic valve EV1, opened suddenly at zero time, from which pressure and temperatures were recorded. Two sets of experiments were performed: (1) in the first, EV2 was closed when the nominal pressure was reached to simu-

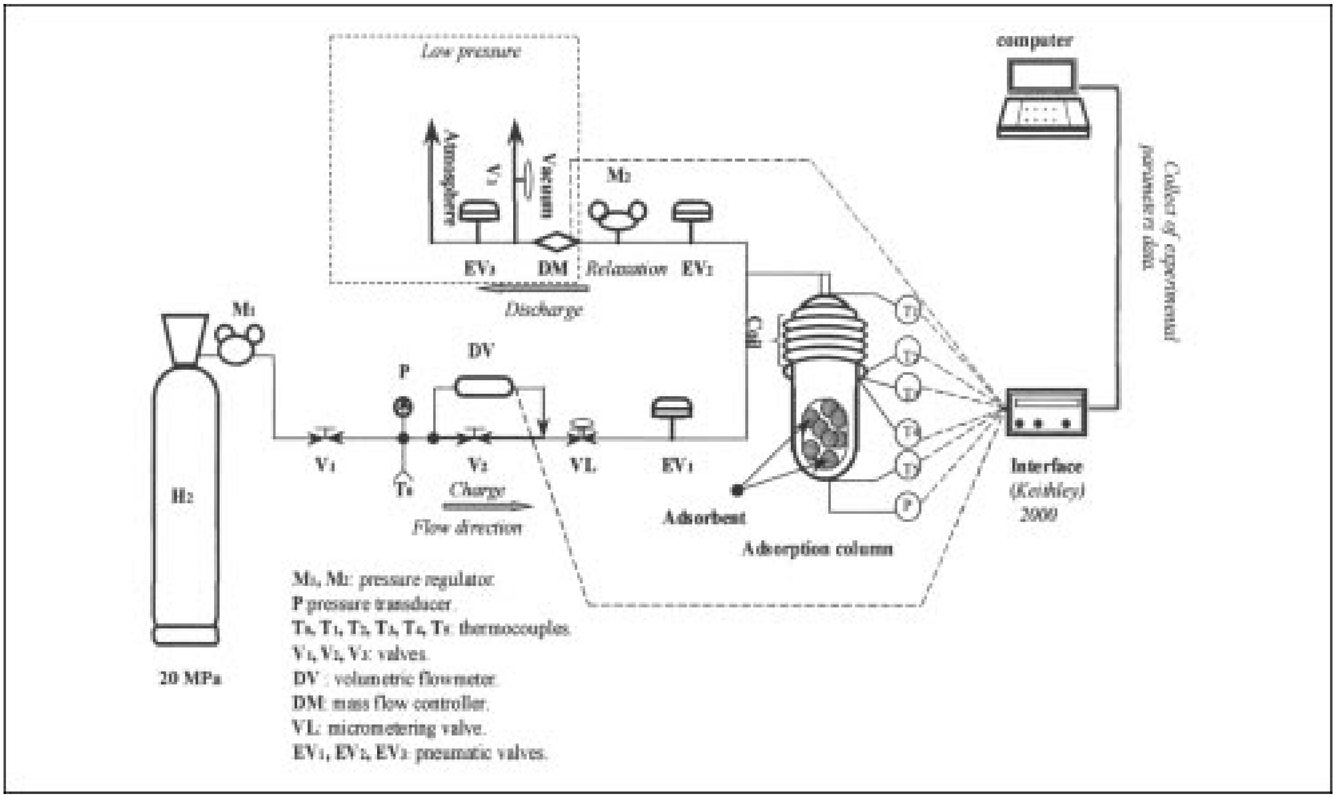

Figure 4. Experimental device for the measurement of adsorption column charge and discharge.

late a real fill-up as for the vehicles; and (2) in the second, the column was charged with hydrogen until the target pressure and thermal equilibrium with the surroundings were achieved (when the temperatures indicated by the thermocouples were equal to the ambient temperature).

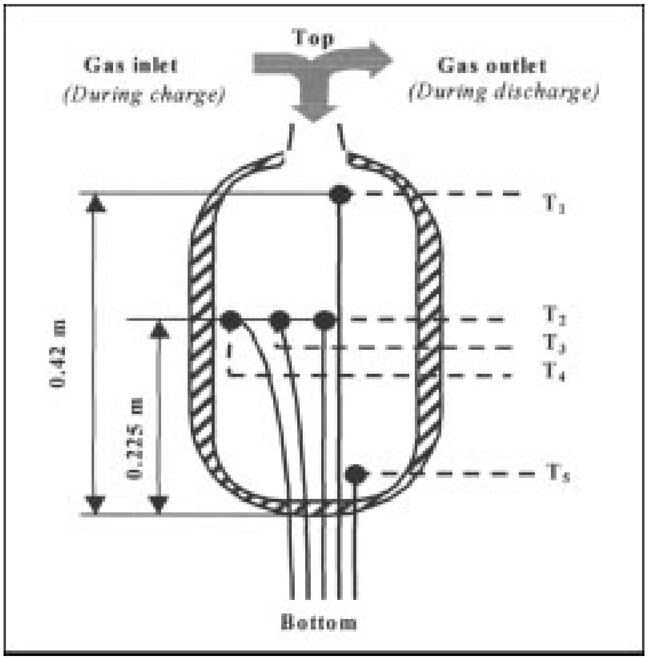

Figure 5. Details of inner column disposition of thermocouples.

Discharge. Since valve EV1 was closed while EV2 and EV3 were opened, the gas was expanded to 0.15 MPa by the pressure regulator (engine operating pressure). Finally, the outlet gas was exhausted through the mass-flow controller.

Presentation and Discussion of Results

Charge

Figure 6 shows typical experimental temperature histories at different radial and axial positions in the bed. These experimental curves were recorded for the three operating pressures ($P = 5$, 10, and 15 MPa) and for three gas flow rates. As expected, in all cases, an increase in temperature was observed, due to both adsorption and compression. The temperature rise magnitude was enhanced by both high pressure and high flow rate. The knowledge of this temperature increase and its dependence on operating conditions is of primary importance for the storage process, as it results in a reduced amount of stored gas, as shown in Figure 7a.

Significant temperature gradients were noted in both the axial and radial directions. These gradients were essentially due to the poor thermal conductivity of the granular adsorbent bed (0.764 W/m·K). As pointed out by Vortmeyer and Winter (1984), in a radial direction, an additional cause might be the bypass flow, because of porosity change near the wall. The bypass flow is relatively important at low flow rates and for low bed-to-particle-diameter ratio ($D_0/d_p = 12$ in our case). According to these authors, at a low Reynolds number

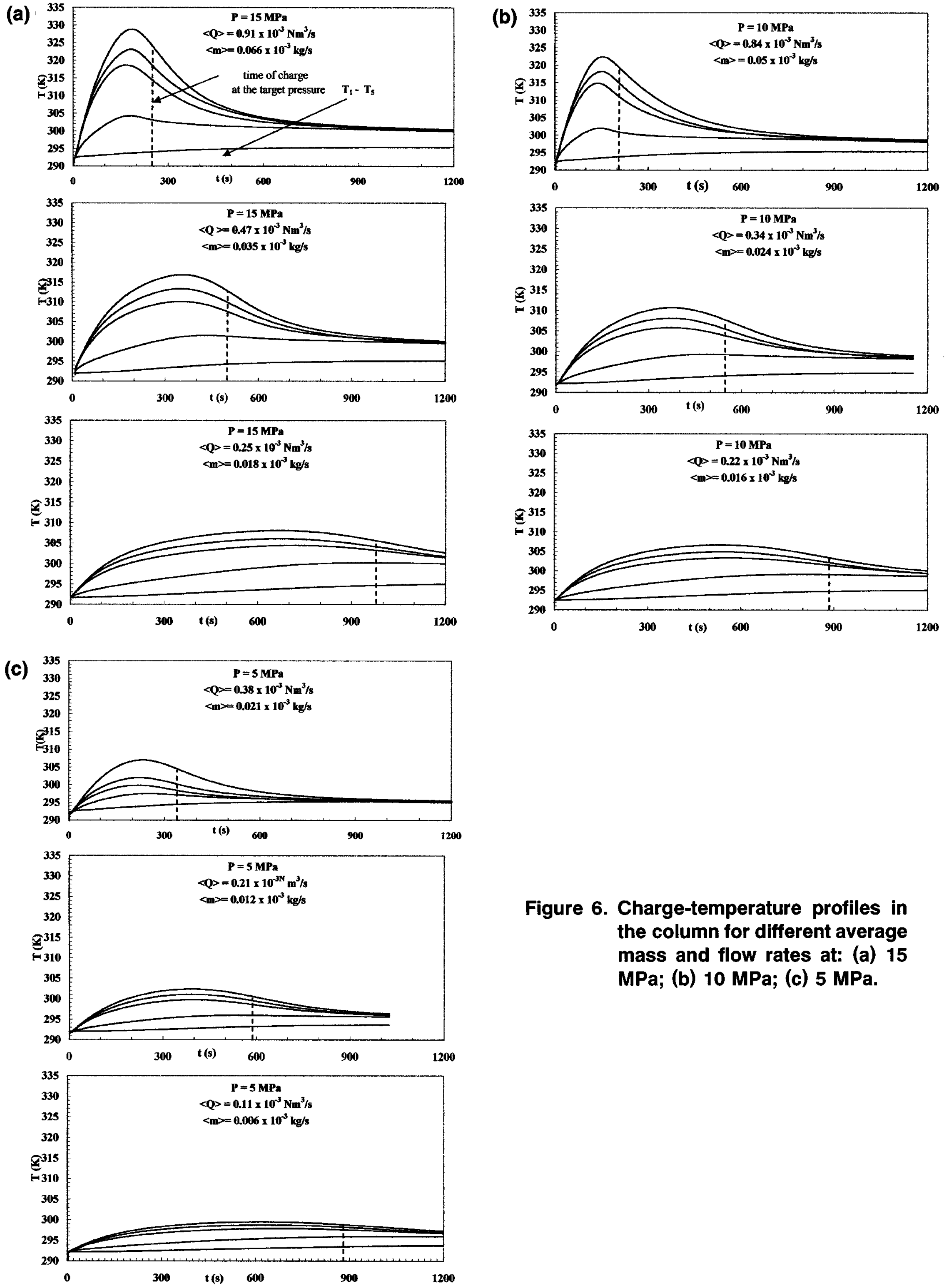

Figure 6. Charge-temperature profiles in the column for different average mass and flow rates at: (a) 15 MPa; (b) 10 MPa; (c) 5 MPa.

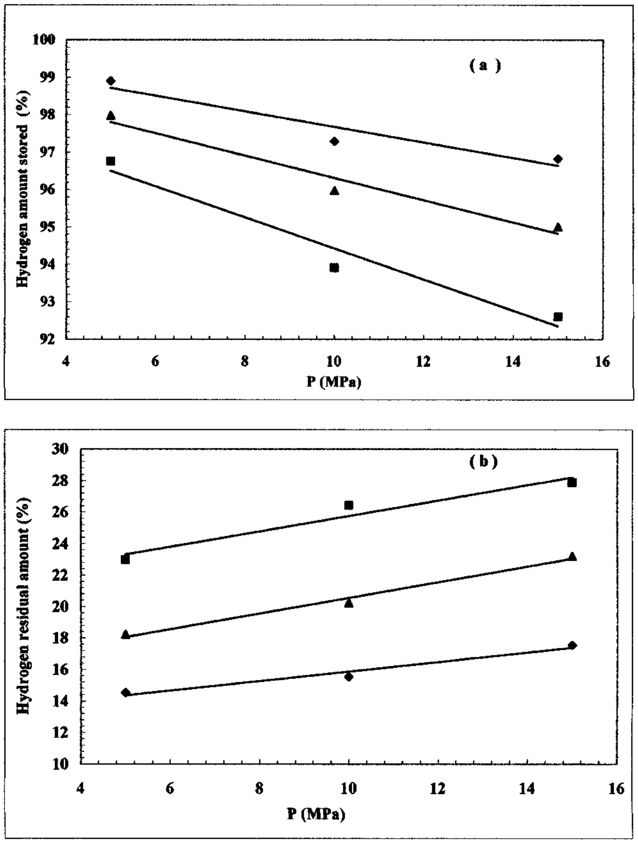

Figure 7. Percentage of mass hydrogen amount (with thermal effect/without thermal effect): (a) stored during charge step; (b) loss during discharge at fast (■), medium (▲), and slow (◆) flow rates for different pressure storage 5, 10, and 15 MPa.

(of 15 and less, in this study), the proportion of flow bypass can reach 30%.

As expected, the highest temperature was obtained near the entrance where gas velocity is more significant. Indeed, this is the region of the bed where the pressurization effect is most important, since hydrogen is gradually adsorbed on activated carbon from the entrance to the bottom bed.

All experimental profiles exhibited a change in curvature, and could be divided into two distinct periods. In the first regime (start period), where $P_2 < 0.53 P_1$ (see Eq. 8), and which is characterized by a rapid temperature rise, the heat generated by adsorption and compression (two exothermic processes) was proportional to the flow rate (convective transport) and the temperature response reached its maximum with a delay corresponding to the inertia of the system. In addition, at low pressure, corresponding to the first charge period, the slope of the adsorption isotherms was steeper than at high pressure (Figure 2). In the second period, the bed was close to saturation, and therefore the flow rate decreased (Eq. 7) and the temperature variation resulted only from conductive heat transfer through the bed and through the steel wall, as well as the convective bed heat exchange with the surroundings. At the final time (1200 s), it is important to note that the bed temperature was different from the ambient temperature and was far from reaching the equilibrium temperature. This was due to heat accumulation in the steel wall, which behaved as a thermal reservoir during this step. Indeed, due to its high heat capacity, the steel wall (about 29 kJ based on experimental results) stored a large part of the heat adsorption generated in the bed (about 27 kJ). It was also observed that the temperature rise at the bottom (thermocouple No. 5) never exceeded 4 K. This was a local effect mainly due to the large mass wall, which was more consequential, and to hardware, such as screws connected in this region, presenting considerable thermal capacity.

Effect of Flow Rate. Considering the three sets of curves in Figure 6[(a) at 15 MPa, (b) 10 MPa, and (c) 5 MPa], it can be noted that the temperature increase at high flow rate is high but of short duration, whereas at low flow rate it is low but of long duration.

For the fast charge conditions, where the system behavior was nearly adiabatic, the heat effect was more pronounced because there was not sufficient time for heat exchange with the surroundings. This implied important temperature gradients in the bed. In fact, the rate of heat generated by adsorption and compression was more rapid than its propagation by convection and conduction, and therefore remained confined to the column. Consequently, important shifts in the adsorption isotherms were also induced by these temperature gradients. For these relatively high flow rates, the average temperature increases were about 40 K at 15 MPa, 21 K at 10 MPa, and 7 K at 5 MPa.

For the slow flow rate the heat exchange with the surroundings could take place and was limited by natural convection outside the wall. In this case, the average temperature rises were between approximately 5 and 7 K. The corresponding percentages of full-charge were between 96 and 98%, only 4% more than the case at fast charge, and therefore there was no definitive advantage to charge with low flow rate. Furthermore, for vehicles, the long filling time—over 900 s—solution was unrealistic and could not be applied.

Effect of Charge Pressure. As expected, lower elevations were obtained at low storage pressure (5 MPa). For the real system, it was obvious that, at this pressure, the amount stored was too low to ensure sufficient autonomy. Nevertheless, the latter experiments, compared to those at 15 MPa, demonstrated that the maximum temperature was obtained in 220 s of charge at 5 MPa (rapid charge case); at 15 MPa this temperature was reached in 75 s. Thus, this implies that the same amount stored at 5 MPa is supplied and accumulated in a shorter time at higher storage pressure. For this reason, we observed a similar temperature rise, despite the difference in the storage pressure, in cases such as for a rapid charge at 5 MPa ($Q = 0.38 \times 10^{-3}$ Nm^3/s) and medium time charge at $P = 10$ MPa ($Q = 0.34 \times 10^{-3}$ Nm^3/s).

Discharge

Figure 8 shows temperature histories for different pressures and fixed discharge flow rates. Contrary to the charge step, a temperature decrease was observed during discharge that was due to both desorption and decompression. Knowledge of the temperature drop was necessary, as it reduced the amount delivered under a given set of operating condi-

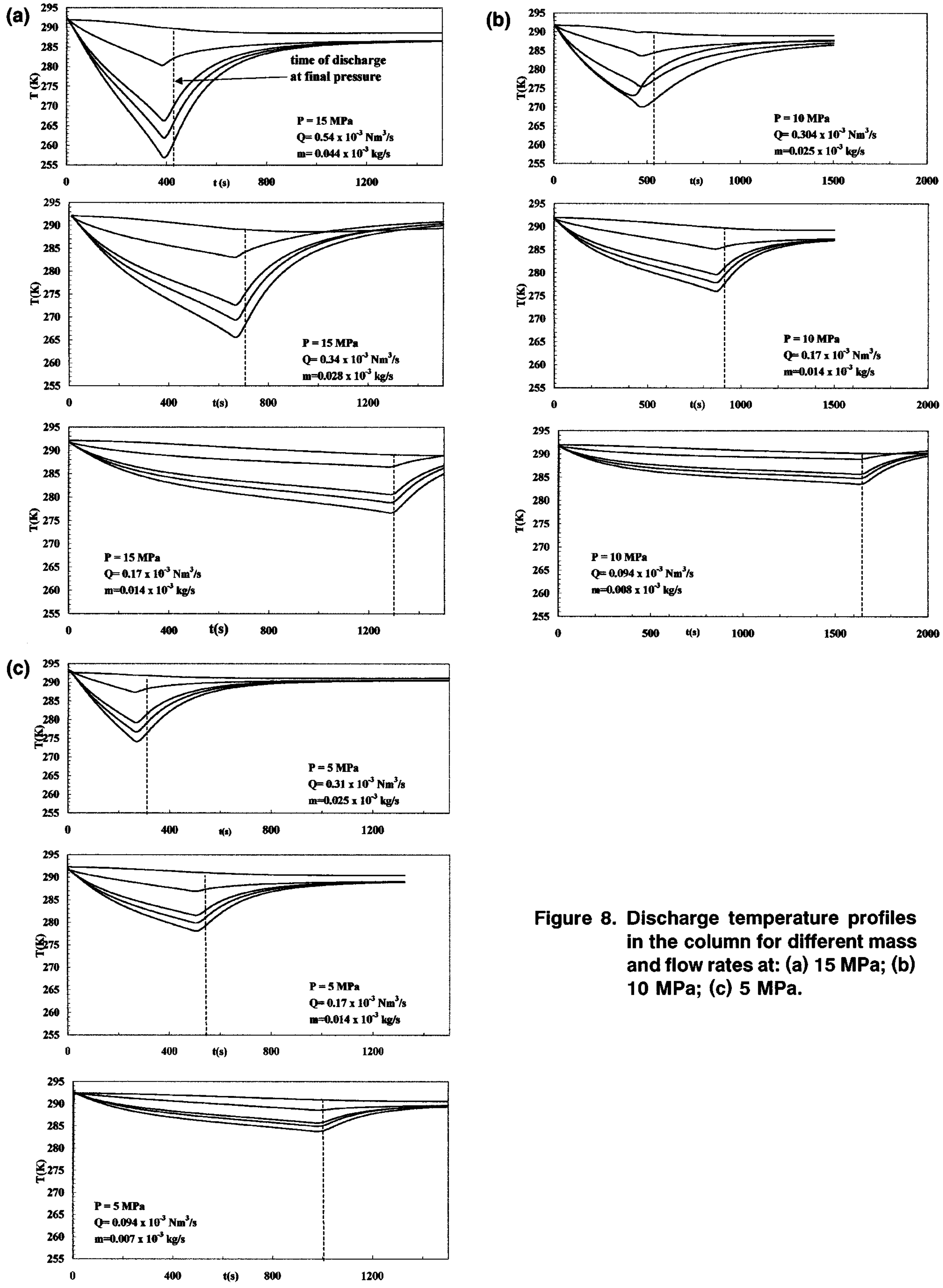

Figure 8. Discharge temperature profiles in the column for different mass and flow rates at: (a) 15 MPa; (b) 10 MPa; (c) 5 MPa.

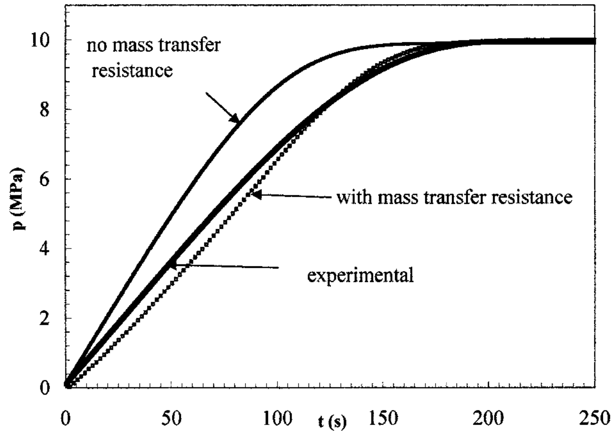

Figure 9. Influence of mass-transfer resistance on the pressure-column history during charge at storage pressure 10 MPa.

tions. The residual amount increased with the pressure and gas flow rate, and varied between 14 and 28%, as shown in Figure 7b.

It is noteworthy that the shape and curvature of temperature curves were not symmetrical to the charge curves. Contrary to charge, as the gas cooled down, an amount was retained, at lower temperature than the ambient temperature. As a result, the desorption path on isotherms was different from the charge path. Furthermore, during this step, the energy stored during pressurization (charge) had to be resupplied to the system.

As for charge, the best operation was accomplished with slow flow rate under hypothetical isotherm conditions (IC). As presented in most of the literature, IC would appear to be more favorable for real operating conditions, while from experimental results and for all cases, it was not possible to operate under this condition only for the infinitely slow flow rate at which the impact of temperature gradients became negligible. For the lowest flow rate, which should be closest to a slow discharge in vehicles (about 50 kW of power), the temperature fell to 277 K at 15 MPa and 287 K at 5 MPa. Calculated from the mass flow controller, the capacity losses were between approximately 15 and 18% (Figure 7b). For the near adiabatic operation (fast discharge), the lowest temperature drop was obtained with a high flow rate operating at 15 MPa. At the end, the wall temperature dropped to about 280 K, while the near-entrance temperature was about 256 K. The volume-average temperature decrease was 30 K. Under these conditions, the equilibrium was unfavorable to total desorption. It had a detrimental effect on performance corresponding to 28% capacity loss. Fortunately, fast discharge was far from vehicle running conditions.

Validation of mathematical models

Charge. Since it was not possible to represent the vast amount of experimental and numerical data obtained at different column positions, we show only the temperature profile for the given thermocouple position T_1 near the entrance to the column. For this thermocouple, we observed the highest temperature rise that was representative of the thermal behavior in the column. The physical parameters used in the calculations are given in Table 2.

First, numerical simulations were performed to investigate the influence of mass-transfer resistance on the final filling time. From Figure 9 it can be seen that the experimental pressure history behaves the same as the computed history, with mass-transfer resistance and particularly near bed saturation. Both the computed and experimental curves coincide perfectly, mainly because mass-transfer resistance has a stronger effect than hydrodynamic flow (contrary to the first regime). In the absence of mass-transfer resistance corresponding to instantaneous equilibrium, nominal pressure is reached earlier with a steeper slope. Therefore, less time is required because 10% less gas is stored.

Figure 10 shows the calculated and experimental temperature rise for thermocouple T_1 at different pressures with different flow rates. For all cases, the agreement between experimental and numerical was good and the maximum temperature elevations were well predicted. The model also provided a very good prediction of the transient behavior at the beginning of charge. It demonstrated that a linear velocity decrease in the bed was a reasonable approximation. Tem-

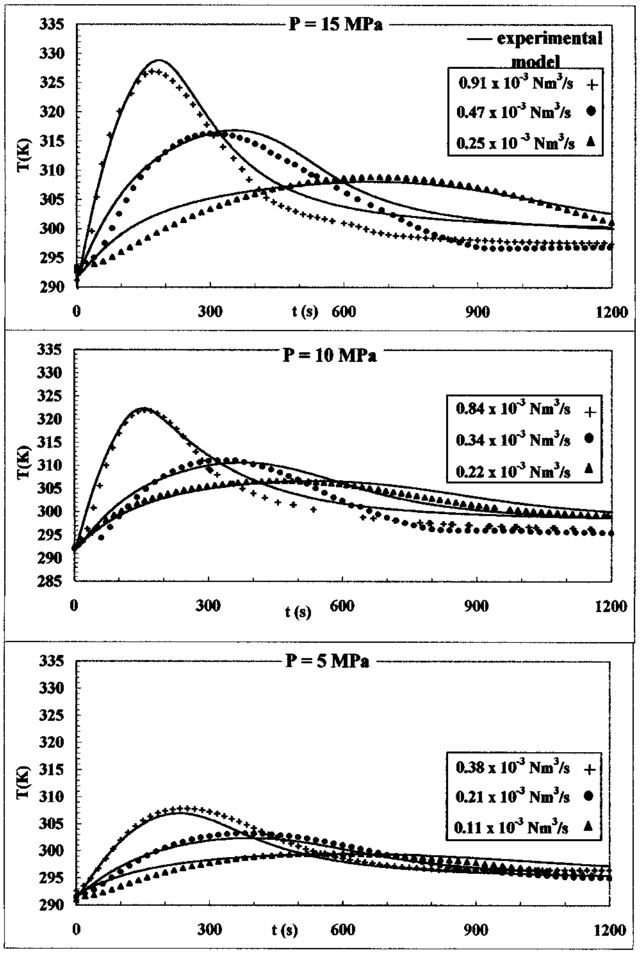

Figure 10. Comparison of model and experimental-bed temperature profiles during charge.

perature histories were most accurately predicted at slow flow rates. However, the prediction of the temperature decrease was less satisfactory at high flow rates. The calculated temperature was slightly lower than the experimental temperature. This difference could be explained by the fact that the model assumes that the bed and wall temperatures are equal. An additional inaccuracy may have been due to the estimation of convection heat transfer coefficient *h* with the surroundings.

Figure 11 shows how the calculated temperature profiles by the idealized model (denoted model 1) will be affected by neglecting the most important energy balance terms. Under adiabatic conditions ($h = 0$), the thermal effect is greater. The heat generated is accumulated in the bed and has nowhere to escape. Thus, a long time is required for temperature stabilization. The maximum temperature was close to that obtained experimentally (5 K more), which confirms that the thermal behavior of the bed during the first charge regime (before temperature maximum) is near the adiabatic one.

In the case where heat accumulation in the wall is neglected (model 3), the temperature maximum is slightly overestimated by about 3 K, compared to model 1. During the second regime (after temperature maximum), the temperature decrease is more rapid toward equilibrium, which is characterized by an absence of a tail, as for model 1. This suggests that the heat released is directly dissipated to the surroundings. This course characterized the wall effect, which behaves like a thermal-energy reservoir, as indicated in the experimental section.

In the last model numerical simulation, the heat generated by compression was assumed to be negligible. The thermal effect was underestimated and the temperature maximum was less by 7 K than the maximum predicted by model 1.

From these runs, it is clear that only the complete model adequately reproduces charge dynamics and can be useful for engineering purposes to predict the temperature rise and to choose operating conditions.

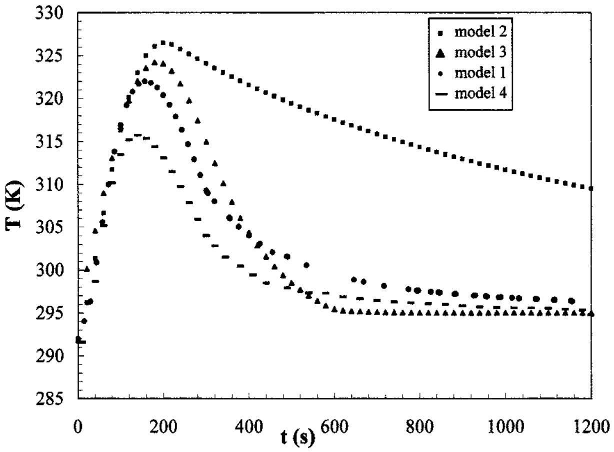

Figure 11. Computed temperature profiles during rapid charge at $P = 10$ MPa showing, respectively, the effects of neglecting.

Model 2: heat transfer with surrounding; model 3: wall heat accumulation; model 4: heat generated by compression; model 1 corresponds to complete charge model.

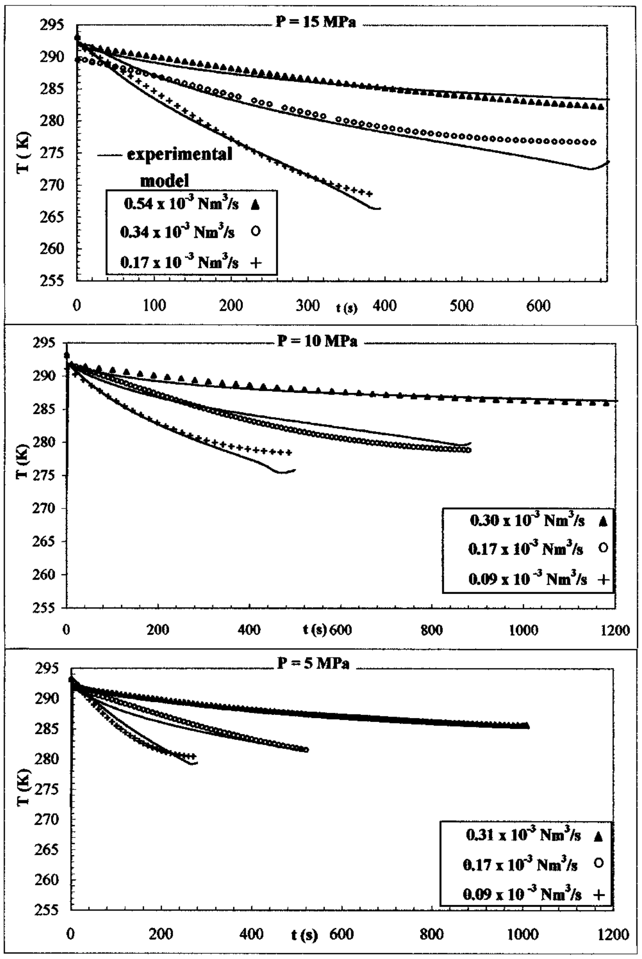

Figure 12. Comparison of model and experimental-bed temperature average profiles during discharge.

Discharge. During this step, the computation of temperature and pressure was maintained until pressure was equal to 0.15 MPa (operating pressure engine). This was the stopping criterion for the discharge computations.

The model and the experimental average temperatures are fairly close in Figure 12. For relatively slow discharge, agreement was very good. At 15 MPa in rapid discharge, the model temperature predicted showed the greatest discrepancy with the measured one. The same observation was also valid for rapid discharge at 10 and 5 MPa. It is difficult to explain the exact reason for this and many explanations can be suggested. The first probably involves neglected mass-transfer resistance. In rapid discharge, the assumption of instantaneous equilibrium becomes erroneous. The second explanation involves the fact that, at these flow rates, the gradient temperature is very high in the column (see the earlier discussion of the experiment). The approximation of uniform temperature and density in an axial direction becomes inaccurate in computations. Nevertheless, the model captures the essence of desorption dynamics: temperature drop for slow flow rates, as for vehicle application.

For this case, Figure 13 shows the effect of neglecting the important terms of the discharge model when predicting the

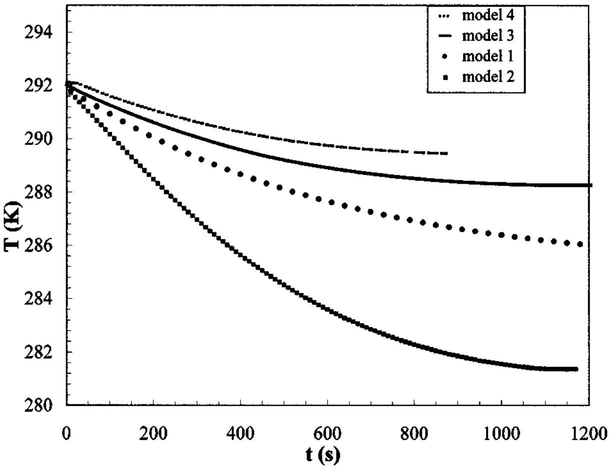

Figure 13. Computed temperature profiles during slow discharge showing, respectively, the effects of neglecting.

Model 2: heat transfer with surrounding; model 3: wall thermal conductivity; model 4: mass accumulation in the bulk phase; model 1 corresponds to complete discharge model.

temperature history. The results are comparable with those previously obtained for the charge model: under adiabatic conditions, the temperature drop is lower than that predicted by model 1. However, a small difference (only 2 K) occurs in the case where wall thermal conductivity is neglected. For a rapid and average discharge time, the effective temperature was declined successively from 8 to 5 K. Another effect associated with the mass accumulation in the bulk phase cited earlier (see the section on mathematical modeling: discharge model) was also demonstrated. The final discharge time at the depletion pressure was not observed, not being as long as in model 1. Thus, the corresponding temperature drop was overestimated and there was only a small amount of gas discharged.

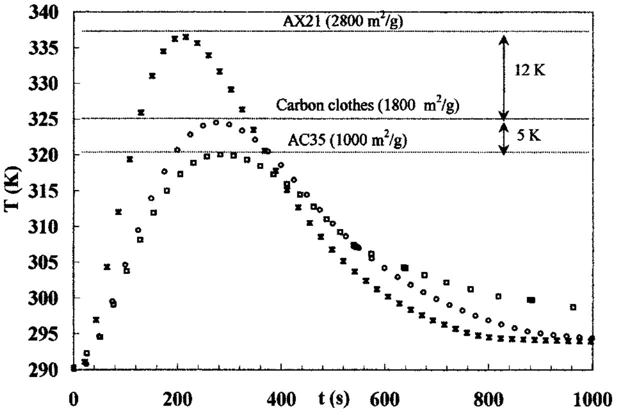

Figure 14. Calculated temperature rise at 10 MPa during rapid charge duration (300 s) using AC35 (□), carbon clothes (○), and AX21 (∗) as adsorbent.

Effects of physical properties of the adsorbent on thermal effects

Experimental results and comparisons with model predictions are specific to carbon AC35 (surface area 1,000 m^2/g), which is produced on a large scale. Superactivated carbon AX21, with a surface area of 2,800 m^2/g (despite its not being commercially available), might be more suitable for optimal storage capacity. Nevertheless, the thermal effects would be enhanced. From the present model predictions, this carbon reaches a higher temperature than AC35 during charge, about 17 K (Figure 14). Thus, it involves a specific device for heat-transfer improvement to maintain optimal storage (otherwise, the capacity losses were 18%). Concerning the carbon clothes (surface area 1,800 m^2/g), the temperature rise was intermediate, between AC35 and AX21.

Another feature must also be taken into account for better adsorbents: the bulk density. Of course, high surface area is desirable in order to maximize the adsorption per unit of mass, but the adsorbent bulk density must be increased. The ideal adsorbent in the vehicular reservoir would have a high bulk density, but would exhibit substantial adsorptivity. It should also have good mechanical properties to avoid attrition.

Conclusion

Two models for the charge and discharge reservoir have been developed here that combine mass and heat balances with a nonlinear isotherm in a packed bed. The proposed models enable the prediction of the behavior of a dynamic storage system for different operating conditions. They were successfully validated under realistic conditions on a laboratory scale with granular activated carbon AC35. Three specific points were considered: (1) time of charge and discharge; (2) charge and discharge step performances; and (3) storage pressure. The models were capable of predicting axial temperature rise during the charge step and radial temperature drop during the discharge step. The model could be used for large-scale reservoirs.

One significant result of this study is that thermal effects reduce the storage capacity during charge and the amount delivered during discharge, and need to be taken into account when applied to vehicles. It also appears that the storage performance of better adsorbents can be reduced because of thermal effects, and enhanced by better adsorption.

Increasing the heat transfer between the bed and the surroundings would reduce this negative effect for real vehicle reservoirs. For this purpose, the following remedies exist.

- In order to enhance radial heat transfer, the gas flow can be radially directed, as suggested by Chang and Talu (1996) for natural gas. The proposed device involves insertion of a fairly small perforated tube into the central axis of the reservoir. The temperature will be more uniform and the storage capacity losses will be decreased compared to the axial flow direction. The second solution is based on an adsorbent package. This package can be disk-shaped with the same radius as the reservoir, and directly in contact with the cylinder wall. Therefore, the void space is reduced, and thermal conductivity and energy transfer through the wall are increased. This suggestion can be sustained, as disk adsorbents are available (Bose et al., 1992).

- To increase the flow of heat to the surroundings during the discharge step, the wall reservoir can be kept externally heated by passing the flow of discharged gases from the motor engine (combustion or fuel cell) through an external jacket. This would avoid an important drop in temperature while the vehicle runs.
- To improve the conductive transfer, the ratio of the wall surface and the volume of the reservoir must be increased. As in the vehicle, the space available is limited, and the reservoir can be divided into several elongated tubes that could also be finned.
- To compensate for the amount of hydrogen lost by overheating during charge, the reservoir can be filled at pressure slightly higher (from 6 to 15%) than the target storage pressure (the percentage depends on the storage pressure).

An interesting development of this study is the optimization of storage by adsorption when the high adsorption capacity of carbon nanotubes and carbon nanofibers is proven true. The developed models can be used as predictive tools in order to find optimum operating conditions for hydrogen storage onboard the vehicle.

Acknowledgments

The authors thank the European Community for financial support under Project "Euro-Quebec Hydro-hydrogen Pilot Project." We acknowledge Professors A. S. Lamine and I. Pentchev for heat-transfer discussions and manuscript suggestions. We also thank D. Vidal, Research Engineer, for his help in the elaboration of the experimental device and K. Paev for his technical contribution.

Notation

$A = A_1 + A_2$, m^2
A_1 = internal area of the column, m^2
A_2 = wall area, m^2
C_p = hydrogen heat capacity, J/kg·K
C_{ps} = carbon heat capacity, J/kg·K
C_{pw} = steel heat capacity, J/kg·K
D_{ax} = axial dispersion coefficient, m^2/s
D_0 = external column diameter, m
D_i = internal column diameter, m
h = external wall heat-transfer coefficient, W/m^2·s
L = length of the column, m
M_{H_2} = molecular mass of hydrogen, kg/kmol
P = pressure, Pa
P_0 = initial pressure, Pa
r = radial position, m
r_p = average particle radius, m
r_g = universal gas constant ($r_g = R/M_{H_2}$), J/kg·K
R = column radius, m
T = temperature, K
T_0 = ambient temperature, K
t = time, s
t_c = cycle time, s
u = interstitial velocity, m/s
w = steel-wall thickness, m
x = axial position, m
ϵ = bed-packing porosity
ρ_s = carbon density, kg/m^3
ρ = gas density, kg/m^3
ρ_0 = gas density at P_0, m^3
ρ_w = steel density, kg/m^3
λ_b = bed effective thermal conductivity, W/m·K
λ_w = wall thermal conductivity, W/m·K
ΔH = heat of adsorption–desorption, J/mol

Subscripts

ax = axial direction
s = adsorbent
w = wall column

Dimensionless groups

Pr = Prandtl number
Re = Reynolds number

Literature Cited

Barbosa, J. P., A. E. Rodriguez, E. Saatdjian, and D. Tondeur, "Dynamics of Natural Gas Adsorption Storage Systems Employing Activated Carbon," *Carbon*, **35**, 12459 (1997a).

Barbosa, J. P., A. E. Rodriguez, E. Saatdjian, and D. Tondeur, "Charge Dynamics of a Methane Adsorption Storage System: Intraparticle Diffusional Effects," *Adsorption.* **3**, 117 (1997b).

Barbosa, J. P., "Modélisation des Transferts Couplés en Milieux Poreux," PhD Thesis, p. 67 (1995).

Berry, D. G., and M. S. Aceves, "On-Board Storage Alternatives for Hydrogen Vehicles," *Energy Fuels*, **12**, 49 (1998).

Bose, T., R. Chahine, and J. M. St-Arnaud, Canadian Patent No. 1310949 (1992).

Brunauer, S., *The Adsorption of Gases and Vapors*, Vol. 1, Princeton Univ. Press, Princeton, NJ, p. 222 (1945).

Chahine, R., and P. Bénard, "Performance Study of Hydrogen Adsorption Storage Systems," *Proc. 12th World Hydrogen Energy Conf.*, p. 979 (1998).

Chahine, R., and T. K. Bose, "Low Pressure Adsorption Storage of Hydrogen," *Int. J. Hydrogen Energy*, **19**, 161 (1992).

Chang, K. J., and O. Talu, "Behavior and Performance of Adsorptive Natural Gas Storage Cylinders During Discharge," *Appl. Therm. Eng.*, **16**, 359 (1996).

Chambers, A., C. Park, R. T. K. Baker, and N. M. Rodriguez, "Hydrogen Storage in Graphite Nanofibers," *J. Phys. Chem. B*, **102**, 4253 (1998).

Chou, C. T., and W. C. Huang, "Incorporation of a Valve Equation into the Simulation of Pressure Swing Adsorption Process," *Chem. Eng. Sci.*, **49**, 75 (1994a).

Chou, C. T., and W. C. Huang, "Simulation of a Four-Bed Pressure Swing Adsorption Process for Oxygen Enrichment Swing Adsorption Process," *Ind. Eng. Chem. Res.*, **33**, 1250 (1994b).

Darkrim, F., J. Vermesse, P. Malbrunot, and D. Levesque, "Monte Carlo Simulation of Nitrogen and Hydrogen Adsorption at High Pressure and Room Temperature," *J. Chem. Phys.*, **110**, 4020 (1999).

Das, L. M., "On-Board Hydrogen Storage Systems for Automotive Application," *Int. J. Hydrogen Energy*, **21**, 789 (1996).

Dillon, A., C. Jones, K. M. Bekkedahl, T. A. Kiang, C. H. Bethune, and M. J. Heben, *Nature*, **386**, (1997).

Farooq, S., M. M. Hassan, and D. M. Ruthven, "Heat Effects in Pressure Swing Adsorption Systems," *Chem. Eng. Sci.*, **43**, 1017 (1988).

Fletcher, C. A. J., *Computational Techniques for Fluid Dynamics*, Springer Series in Computational Physics, Vol. 1, Springer-Verlag, New York, p. 183 (1991).

Froment, G. F., and K. B. Bischoff, *Chemical Reactor Analysis and Design*, Wiley, New York, p. 456 (1990).

Glueckauf, E., "Theory of Chromatography, Part 10 Formula for Diffusion into Spheres and Their Application to Chromatography," *Trans. Faraday Soc.*, **54**, 1540 (1955).

Gunn, D. J., "Axial and Radial Dispersion in Fixed Beds," *Chem. Eng. Sci.*, **42**, 361 (1987).

Hassan, M. M., N. S. Raghavan, D. M. Ruthven, and H. A. Boniface, "Pressure Swing Adsorption—II," *AIChE J.*, **31**, 2008 (1985).

Hirschfelder, O. J., F. C. Curtiss, and B. R. Bird, *Molecular Theory of Gases and Liquids*, Wiley, New York, pp. 538, 1126 (1964).

Hynek, S., W. Fuller, and J. Bentley, "Hydrogen Storage by Adsorption," *Int. J. Hydrogen Energy*, **22**, 601 (1997).

Kikkinides, E. S., and R. T. Yang, "Effects of Bed Pressure Drop on Isothermal and Adiabatic Adsorber Dynamics," *Chem. Eng. Sci.*, **48**, 1545 (1993).

Kumar, R., "Adsorption Column Blowdown: Adiabatic Equilibrium

Model for Bulk Binary Gas Mixtures,'' *Ind. Eng. Res.*, **28**, 1677 (1989).

Lamari, M., A. Aoufi, P. Malbrunot, and I. Pentchev, ''Storage of Hydrogen by Adsorption at Room Temperature: Realistic Way of Storage,'' *Proc. 8th Canadian Hydrogen Workshop*, p. 352 (1997).

Lamari, M., K. Paev, and P. Malbrunot, ''Measurement of the Effective Thermal Conductivity of Stagnant Carbon Bed at High Pressure,'' *Chem. Eng. Sci.* (1999).

Lu, Z. P., J. M. Luriero, and M. D. LeVan, ''Pressurization and Blowdown of Adsorption Beds,'' *Chem. Eng. Sci.*, **48**, 1699 (1993).

Malbrunot, P., D. Vidal, J. Vermesse, R. Chahine, and T. K. Bose, ''Adsorbent Helium Density Measurement and Its Effect on Adsorption at High Pressure,'' *Langmuir*, **13**, 539 (1997).

Malbrunot, P., D. Vidal, and J. Vermesse, ''Storage of Gases at Room Temperature by Adsorption at High Pressure,'' *Appl. Therm. Eng.*, **16**, 375 (1996).

Nicholetti, G., ''The Hydrogen Option for Energy: A Review of Technical, Environmental and Economic Aspects,'' *Int. J. Hydrogen Energy*, **20**, 759 (1995).

Noh, J. S., R. K. Agawal, and J. A. Schwartz, ''Hydrogen Storage Using Activated Carbon,'' *Int. J. Hydrogen Energy*, **12**, 693 (1987).

Radke, C. J., and J. M. Prausnitz, ''Thermodynamics of Multi-Solute Adsorption from Dilute Solutions,'' *AIChE J.*, **18**, 761 (1972).

Rodriguez, N. M., and T. K. Baker, ''Storage of Hydrogen in Layered Nanostructures,'' US Patent No. 5 653 951 (1997).

Ruthven, M., S. Farooq, and K. Knaebel, *Pressure Swing Adsorption*, VCH, p. 36 (1994).

Sundaram, N., and P. Wanket, ''Pressure Drop Effects in the Pressurization and Blowdown Steps of a Pressure Swing,'' *Chem. Eng. Sci.*, **43**, 123 (1988).

Vortmeyer, D., and R. P. Winter, ''Improvements in Reactor Analysis Porosity and Velocity Profiles,'' *Ger. Chem. Eng.*, **7**, 19 (1984).

Yang, R. T., *Gas Separation by Adsorption Processes*, Butterworth, Boston, p. 127 (1987).

Yang, R. T., and R. Liu, ''Gaseous Diffusion in Porous Solids at Elevated Temperatures,'' *Ind. Eng. Chem. Fundam.*, **21**, 262 (1982).

Zhong, G. M., F. Meunier, S. Huberson, and J. B. Chalfen, ''Pressurization of a Single Component Gas in an Adsorption Column,'' *Chem. Eng. Sci.*, **47**, 543 (1992).

Manuscript received June 4, 1999, and revision received Nov. 1, 1999.